Dynamic Sealing Using Magnetorheological Fluids

Youzhi Liang, Jose R. Alvarado, Karl D. Iagnemma, and A.E. Hosoi

Phys. Rev. Applied **10**, 064049 — Published 20 December 2018

DOI: 10.1103/PhysRevApplied.10.064049

Dynamic Sealing Using Magneto-Rheological Fluids

Youzhi Liang,* Jose R. Alvarado, Karl D. Iagnemma, and A. E. Hosoi

Department of Mechanical Engineering,
Massachusetts Institute of Technology,
77 Massachusetts Avenue, Cambridge,
Massachusetts 02139, USA

(Dated: December 4, 2018)

Micropumps are microfluidic components which are widely used in applications such as chemical analysis, biological sensing and micro-robots. However, one obstacle in developing micropumps is the extremely low efficiency relative to their macro-scale counterparts. This paper presents a dynamic sealing method for external gear pumps to reduce the volumetric losses through the clearance between the tips of gears and the housing by using magneto-rheological (MR) fluids. By mitigating these losses, we are able to achieve high efficiency and high volumetric accuracy with current mechanical architectures and manufacturing tolerances. Static and dynamic sealing using MR fluids are investigated theoretically and experimentally. Two Mason numbers $Mn\,(p)$ and $Mn\,(\Omega)$ which are defined in terms of pressure gradient of the flow and velocity of the moving boundary respectively are used to characterize and evaluate the sealing performance. A range of magnetic field intensities is explored to determine optimal sealing effectiveness, where effectiveness is evaluated using the ratio of volumetric loss and friction factor. Finally, we quantify the effectiveness of this dynamic sealing method under different working conditions for gear pumps.

I. INTRODUCTION

Micropumps are miniaturized pumping devices that are usually manufactured by MEMS micromachining technologies [1, 2]. In recent years, the target applications have expanded owing to the integration of novel physical principles and the invention of new fabrication methods. Micropumps are commonly used in chemical analyses, biological sensing, drug delivery and micro-robots [3–5].

Unfortunately, miniaturization comes at a cost and nearly all micropumps suffer from low efficiency. The reported efficiencies of the available micropump technologies are shown in Fig. 1. Typically, the overall efficiency of a micropump is determined by a combination of four components: volumetric efficiency, hydraulic efficiency, mechanical efficiency and electrical efficiency. Out of these four, volumetric losses and hydraulic losses dominate at small scales. As the size of the system decreases, the volumetric efficiency decreases since the same dimensional and geometric tolerances result in a larger fractional loss. Furthermore, in terms of hydraulic efficiency, the Reynolds number decreases as the system's size decreases, resulting in larger viscous losses.

For external gear pumps, the volumetric losses are roughly proportional to the pressure gradient assuming a quasi-steady fully developed low Reynolds number flow across the clearance between the housing and the gear tips [19]. Thus, the efficiency may be extremely low when the pump is operating under high pressure gradient conditions. The volumetric leakage between the tips of the gears and across the side plates is typically considered to comprise the largest proportion of the total efficiency loss in external gear pumps [20, 21]. Various end wear plates have been studied and designed to reduce the leakage

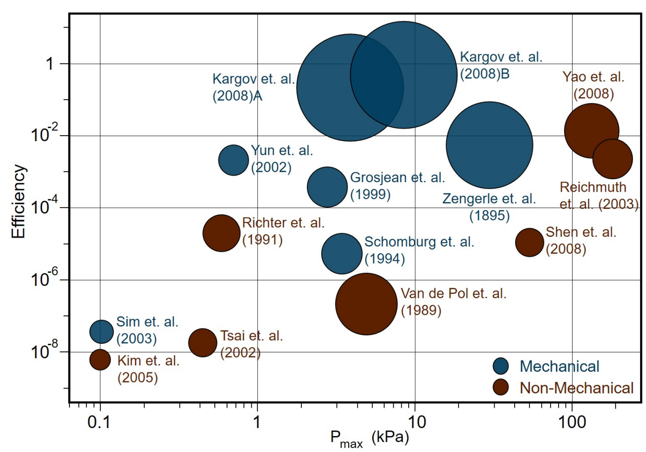

FIG. 1. Review of efficiency versus maximum pressure for existing small-scale pumping strategies. The size of the symbol depicts the characteristic length scale of the pump package; the location of the center depicts the effeciency versus the pressure. For reference, Sim *et. al* is 72 mm^3 and Kargov *et. al* is 18.5 cm^3. Pumps shown here include: Sim *et. al*: Micropump with flap valves [6], Kim *et. al*: Electromagnetic pump [7], Yun *et. al*: Surface-tension driven pump [8], Richter *et. al*: Electrohydrodynamic pump [9], Tsai *et. al*: Thermal-bubble-actuated pump [10], Kargov *et. al*: Gear pump [11], Grosjean *et. al*: Thermopneumatic pump [12], Schomburg *et. al*: Pneumatic chamber pump [13], Van de Pol *et. al*: Thermopneumatic pump [14], Zengerle *et. al*: Electrostatic pump [15], Shen *et. al*: Electromagnetic pump [16], Yao *et. al*: Electroosmotic pump [17], Reichmuth *et. al*: electrokinetic pump [18].

* Corresponding author
YOUZHIL@mit.edu

across the side plates [22]. However, studies that consider volumetric losses between the tip of the gear teeth and the housing are relatively rare. Sealing is even more challenging for micro-scale gear pumps due to the limits of manufacturing precision. With precise manufacturing techniques and tight tolerances, the volumetric loss could be reduced. But in that case the mechanical friction between the housing and the gears will increase and small clearances may also make the pump more vulnerable to vibrations. Therefore, we propose to develop a dynamic sealing method using magneto-rheological (MR) fluids that can operate with the current mechanical architectures and manufacturing tolerances.

Magnetorheological (MR) fluids are materials that exhibit a reversible change in rheological properties with the application of an external magnetic field, which can result in a rich range of physical properties [23–26]. In engineering applications, they were initially used by Jacob Rabinow in the design of a clutch in the late 1940s [27]. In more recent years, MR fluids have found further applications and commercial success [28]. The most common application is a mechanical damper, which yields appealing features such as low-power consumption, force controllability and rapid response [29, 30]. In particular, automotive dampers with these properties have been widely investigated [29, 31, 32]. The other common use of MR fluids is the development of MR valves. In addition, high efficiency, miniaturized MR valves have been achieved [33, 34].

A schematic of a typical external gear pump is shown in Fig. 2. The pressure of the outlet is larger than that of the inlet, resulting in back-flow across the gap between the tips of the gears and the pump housing, as shown in Fig. 2 (b). Subjecting MR fluid to an external magnetic field causes magnetic-induced dipoles to aggregate in the vicinity of the housing, which prevents back-flow (Fig. 2 (c)). This design has the potential to control the clearance between the housing and gear tips without requiring high precision manufacturing techniques.

Previous research primarily focused on MR fluids in either Couette flow or Poiseuille flow, usually within the scope of high shear stress which arises from either a large pressure differential or large exerted force [24, 26–35]. By contrast, much less is known about the physics of MR fluids subject to the combination of Couette and Poiseuille flow. In this study, we investigate the performance of dynamic seals of MR fluid chains subject to shear-driven flows from gear motion and simultaneously to pressure-driven flows from back-flow. We compare experimental results to a model which incorporates two dimensionless Mason numbers, one from Couette flow and one from Poiseuille flow.

II. METHOD

A. Experiments for MR Fluid in Poiseuille Flow or Couette Flow

In order to visualize the effect of Poiseuille flow on the morphology of the MR chains, we designed a experimental system specialized for visualization. We built a micro-channel network made of a silicon slide, which is laser-cut and sandwiched between two transparent acrylic plates. MR fluid is from Lord. The carrier fluid of the MR fluids is silicone oil (Gelest, 100cSt). The volume fraction of MR particles is diluted to be 1%. The particles of MR fluids are made of iron with a surfactant coating to mitigate agglomeration; the diameter of the particles ranges between 1 μm to 20 μm. The fluid exhibits paramagnetic behavior. The flow was driven by a pressure gradient using a syringe pump to control the flow rate. Typical structures in the channel, i.e., chains of particles for different flow rates are displayed in Fig. 3 (Top). The images suggest that the deformation of the magnetic chains increases as flow rate increases until the magnetic chains finally collapse. Note that with low flow rate, magnetic chains tend to aggregate in bunches with very little deformation. These chains appear to attach in the vicinity of the walls of the channel. As the flow rate increases, the chains are more clearly deformed and segregated.

To observe the deformation of MR chains under Couette flow, we built another experimental system. We run the experiments without an adverse pressure gradient. Results are shown in Fig. 3 (Bottom); the left black area of each figure depicts a roughened stationary surface, and the black line on the upper right depicts the surface of a disk. As the rotational speed of the disk increases, the

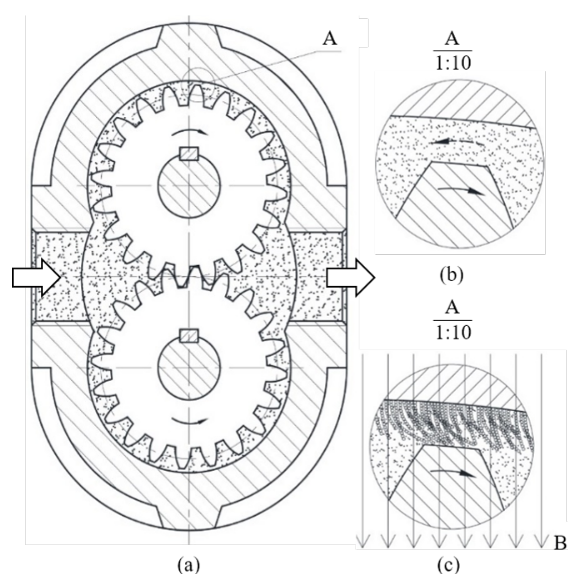

FIG. 2. (a) Schematic of an external gear pump; (b) Volumetric loss caused by back-flow in-between the gear tooth and the housing (indicated by the dashed arrow); (c) Proposed dynamic sealing method using MR fluids in presence of magnetic field B.

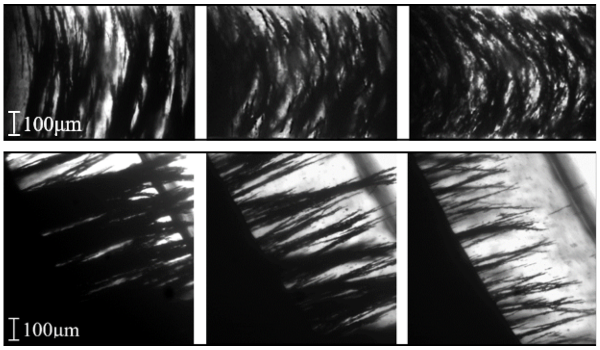

FIG. 3. (Top) Deformation of chains of induced dipoles in Poiseuille flow. (Bottom) Deformation of chains of induced dipoles in Couette flow. (The contrast of the pictures has been enhanced.) (Top) Flow rates from the left to the right: 0.1 ml/min, 1 ml/min, 10 ml/min. Channel width: 0.7 mm. (Bottom) Rotational speed from the left to the right: 0 rps, 0.4 rps, 0.8 rps. Radius of the disk: 25 mm, Channel width: 0.7 mm.

density of magnetic brushes decreases and the curvature of the chains increases.

B. Experiments for MR Fluid in Poiseuille-Couette Flow

To model the interaction between the gear tooth and the housing, we built a simplified experimental system, as shown in Fig. 4. Panel (a) depicts a schematic of the underlying design, where fluid enters the inlet on the left, then bifurcates into two slots. The slot is used to mimic the clearance between the tip of the gears and the housing. A rotating disk is utilized to mimic one gear tooth.

Fig. 4 (b) and (c) show snapshots of the experimental model system, which mainly consists of a frame, a motor, a disk, two pitot tubes, a magnet and two pressure sensors. The frame, which is designed to secure other components, contains a cavity, which connects the tube fitting, the pitot tube and the tube connected to the slots in the middle. A laser cut acrylic disk, driven by the motor, is sandwiched between two transparent plates with slots to secure the magnet. The carrier fluid of the MR fluids is silicone oil (Gelest, 100 cSt). MR fluid is from Lord. The volume fraction of MR particles is diluted to be 10%. The magnets have a surface field of 1895 Gauss (NdFeB, Grade N42, 2.44 oz.). Details of the magnetic field are included in Appendix B.

We used a variable voltage power supply to power both the sensors and the motor (Pololu 12 V), using voltages of 10.5 V and from 0 V to 40 V respectively. Pressure data acquired from the sensors were sent to Labview via National Instruments I/O. Motor speed was acquired from the encoder of the motor and sent to the Arduino built-in serial monitor via Arduino Uno.

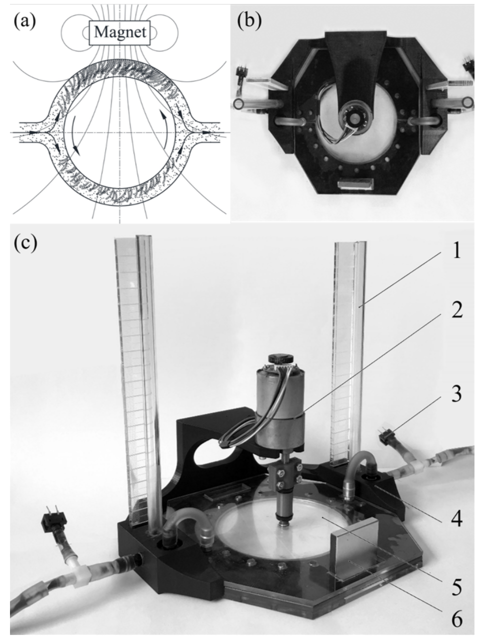

FIG. 4. (a) Schematic of the experiment designed to study the dynamic sealing performance using MR fluid; (b) Top view of the experimental setup. (c) Perspective view of the experimental setup. 1: pitot tube, 2: motor, 3: pressure sensor, 4: frame, 5: disk (inside), 6: magnet.

III. RESULTS AND DISCUSSION

A. Model for MR Fluid in Poiseuille-Couette Flow

The experimental setup, shown in Fig. 4, can be modeled as two slots in parallel in the presence of variable magnetic field intensity. A schematic of one slot is shown in Fig. 5. This half can be simplified as a straight channel with the reference frame attached shown in the partial enlarged view in Fig. 5, based on the fact that the aspect ratio $\delta/R = 2$ mm/50 mm $\ll 1$ (see Appendix B). Thus, we consider two straight slots in parallel. The theoretical results are calculated numerically to account for the square channel cross-section [36]. The Reynolds number $Re_\delta = \frac{\rho U \delta}{\mu} = 0.05 \ll 1$, so the inertia of the MR fluid is negligible.

The flow is driven by both a pressure gradient and a moving wall. In the limit of low Reynolds number, the conservation of momentum equation for steady, laminar flow, in the x-direction, reduces to:

$$\frac{dp}{dx} = \frac{d\tau_{yx}}{dy}, \tag{1}$$

where p is the mechanical pressure, τ_{yx} is the shear stress.

The MR fluid is modeled as a Bingham fluid (see Appendix C for other constitutive relationships). Due to the distribution of magnetic field intensity, the yield stress is larger in the slot closer to the magnet than that in the further one. The constitutive relationship can be expressed

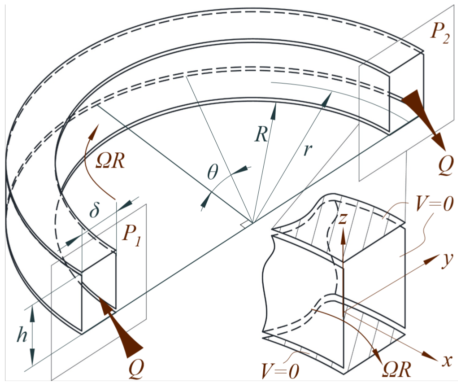

FIG. 5. Schematic of one slot. In the experiment, the radius of the inner annuli is $R = 50$ mm, the width of the slot is $\delta = 2$ mm, the height is $h = 4$ mm. The inner annulus rotates at angular velocity of ΩR; the outer annulus is stationary. P_1 and P_2 denote different pressures.

as:

$$\tau_{yx} = \left(\mu + \frac{\tau_y(\theta)}{|\dot{\gamma}|}\right)\dot{\gamma}; |\tau| > \tau_y(\theta) \qquad \dot{\gamma} = 0; |\tau| \le \tau_y(\theta), \tag{2}$$

where μ is the effective viscosity of the MR fluid, $\tau_y(\theta)$ is the yield stress, and $\dot{\gamma}$ is the shear rate. We furthermore have the following boundary conditions on the inner and outer walls of the channel:

$$v_x|_{y=0} = U \qquad v_x|_{y=\delta} = 0, \tag{3}$$

where v_x is the velocity of the fluid in x-direction and U is the velocity of the inner wall.

To characterize the behavior of the dipole chains, we use the Mason number, which has been commonly considered in prior studies [37–40]. In our study, we define two Mason numbers: one which is the ratio between the shear forces and the magnetic interaction forces in Poiseuille flow, and another one for Couette flow. The magnetic interaction forces are characterized by the yield stress τ_y [41, 42].

$$Mn\,(p) = \frac{\delta}{\tau_y}\left(-\frac{dp}{dx}\right) \qquad Mn\,(\Omega) = \frac{\tau_y \delta}{\mu R \Omega}. \tag{4}$$

To non-dimensionlize the governing equation, the other dimensionless variables are defined as follows:

$$y^* = \frac{y}{\delta}; \tau^* = \frac{\tau_{yx}}{\tau_y}; v^* = \frac{v_x}{R\Omega}; U^* = \frac{R\Omega}{|R\Omega|}. \tag{5}$$

Thus, U^* is either 1 or -1. Substituting the dimensionless variables into the conservation of momentum equation

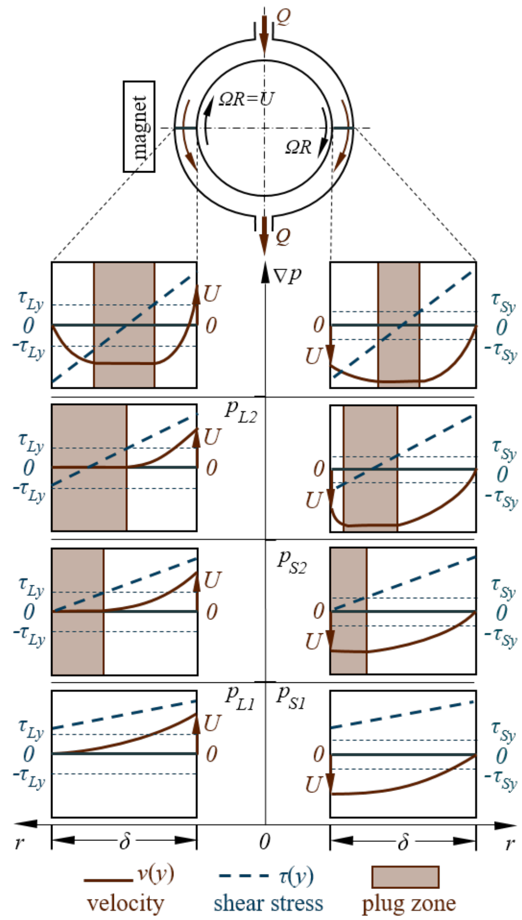

FIG. 6. Schematic of the profiles for velocity, shear stress and plug zone of Poiseuille-Couette flow of MR fluid in both slots, exposed in larger magnetic field intensity (left) and smaller magnetic field intensity (right) respectively, as pressure gradient ∇P increases. δ indicates the width of the channel; the arrow in the profile plots indicates the velocity U of the moving wall. p_{L1} and p_{L2} represent the transition pressure from the one-region mode to the two-region mode and from the two-region mode to the three-region mode respectively, in the presence of larger magnetic field intensity; p_{S1} and p_{S2} represent those in the presence of smaller magnetic field intensity.

and the constitutive equation yields:

$$\frac{d\tau^*}{dy^*} + Mn\,(p) = 0; \qquad \tau^* = \frac{1}{Mn\,(\Omega)}\frac{dv^*}{dy^*} + sgn\left(\frac{dv^*}{dy^*}\right); |\tau^*| > 1 \qquad \frac{dv^*}{dy^*} = 0; |\tau^*| \le 1. \tag{6}$$

The boundary conditions become:

$$v^*|_{y^*=0} = U^*; v^*|_{y^*=1} = 0. \tag{7}$$

The velocity profiles (see Appendix A for details) can be computed from the governing equation and the associated boundary conditions, and can be categorized into three modes: (i) a one-region mode, (ii) a two-region mode and (iii) a three-region mode [43, 44]. (i) The one-region mode occurs when the pressure gradient is small and the velocity of the boundary is relatively large. The fluid stress is larger than the yield stress of the Bingham fluid across the entire slot, so MR chains cannot form. The velocity profile in the one-region mode is identical to that of a Newtonian fluid in Poiseuille-Couette flow. (ii) The two-region mode occurs as the pressure gradient increases, which increases the slope of the stress distribution. In the region where the fluid stress is smaller than the yield stress, a plug zone will occur, where MR chains form and the velocity profile resembles plug flow. In two-region mode, the plug zone is anchored to the surface nearest the magnet, whereas in the region at the opposing surface the MR particles are prevented from aggregating, similarly to one-region mode. (iii) Finally, the three-region mode occurs as the pressure gradient increases even further. Under such conditions, the plug zone will detach from the wall and move to the middle of the channel, surrounded by Newtonian regions on either side. Considering these three types of modes for the two slots in our experimental study, there are four possible combinations of velocity profiles in this study, as shown in Fig. 6. The slot closest to the magnet is in the presence of a higher magnetic field, resulting in a larger yield stress τ_{Ly}.

The average velocity of the fluid in the one-region mode is given by:

$$\overline{v}^* = \frac{1}{12} Mn\,(\Omega)\, Mn\,(p) + \frac{1}{2} U^*. \tag{8}$$

The average velocity of the fluid in the two-region mode depends on the sign of $Mn(p)$ and $Mn(\Omega)$. When $Mn(p)$ has the same sign as $M(\Omega)$, we have:

$$\overline{v}^* = U^* - \frac{U^*}{3}\sqrt{\frac{2U^*}{Mn\,(\Omega)\, Mn\,(p)}}. \tag{9}$$

and when $Mn(p)$ has the opposite sign to $Mn(\Omega)$, we have:

$$\overline{v}^* = \frac{U^*}{3}\sqrt{\frac{-2U^*}{Mn\,(\Omega)\, Mn\,(p)}}. \tag{10}$$

The average velocity of the fluid in the three-region mode is given by:

$$\begin{aligned}\overline{v}^* =& \frac{1}{12} Mn\,(\Omega)\, Mn\,(p)\left(1 - \frac{3}{|Mn\,(p)\,|} + \frac{4}{|Mn\,(p)\,|^3}\right)\\ &+ \frac{U^*}{2} \pm \frac{1}{Mn(\Omega)(2 \mp Mn(p))^2}.\end{aligned} \tag{11}$$

The transition pressure from the one-region mode to the two-region mode and from the two-region mode to the three-region mode can also be computed and are found

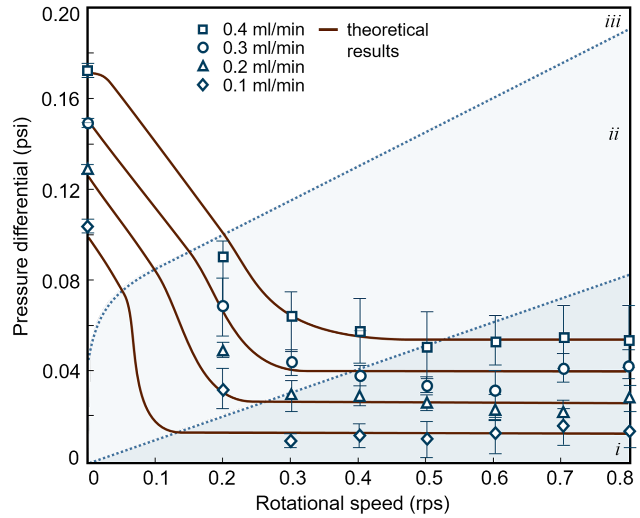

FIG. 7. Experimental and theoretical results. Pressure differential (psi) as a function of rotational speed (rps), for flow rates from 0.1 ml/min to 0.4 ml/min. Each point corresponds to the mean from three iterations of experiments, with error bars indicating standard deviation. *i*: one-region mode; *ii*: two-region mode; *iii*: three-region mode.

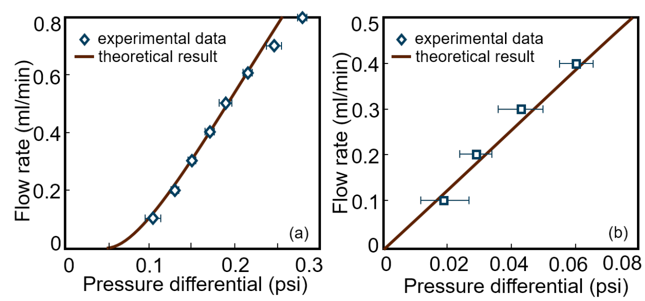

FIG. 8. Experimental data and theoretical results of two limiting cases of Poiseuille flow of MR fluids (a) as Bingham fluid when rotational speed of the disk is zero, and (b) in one-region mode when the rotational speed is sufficiently large. Flow rates (ml/min) as a function of pressure differential (psi).

to be quantities $Mn(p)_{R1}$ and $Mn(p)_{R2}$ respectively:

$$Mn(p)_{R1} = \frac{2}{Mn(\Omega)} \tag{12}$$

$$Mn(p)_{R2} = 2 + \frac{1}{Mn(\Omega)} + \sqrt{\frac{1}{Mn(\Omega)^2} + \frac{4}{Mn(\Omega)}} \tag{13}$$

B. Experimental Results for MR Fluid in Poiseuille-Couette Flow

We investigate the performance of the dynamic seals using the experimental setup shown in Fig. 4 (b). The flow rate is controlled by a syringe pump, ranging from 0.1 ml/min to 0.8 ml/min. For each given flow rate, the rotational speed of the motor is varied from 0 rps to 0.8 rps. The pressure differential is given by two pressure sensors located at the inlet and the outlet. The results are shown in Fig. 7 (a). As the rotational speed increases, the pressure differential decreases abruptly from the static state to the dynamic state, and settles to a steady state.

We apply numerical methods to calculate the velocity profile in the rectangular cross-section, and integrate the velocity profile in the cross-section to get the total flow rate. We first consider Couette flow as a simple example. In the case of two parallel infinite plates, the velocity decreases linearly away from the moving wall. In the experimental setup, as shown in Fig. 4 and Fig. 5, the aspect ratio $h:\delta = 4$ mm: 2 mm$= 2:1$ with a clearance 0.127 mm due to the gasket for sealing. In our experiments, a significant pressure loss occurs due to the Poiseuille flow between the sensors and the inlet and outlet, four 90°-elbows and the cavities which connect the pitot tube and the two tubings (see Appendix B).

A comparison of our mathematical Bingham model with experimental measurements is shown in Fig. 8. One limiting condition occurs when the rotational speed is zero, which corresponds to the classic Poseuille flow for a Bingham fluid. In our experiment, this condition can be treated as two slots for Bingham Poiseuille flow in parallel with different yield stresses $\tau_y(\theta)$ (Fig. 8 (a)). The other limiting condition occurs when the rotational speed of the disk is fast enough so that the flow in both slots are in the one-region mode. Thus, the velocity profile of MR fluid is identical as that of Poiseuille-Couette flow of a Newtonian fluid. Because the directions of the Couette flow are opposite in the parallel slots, the flow rate induced by Couette flow is canceled out. Thus, the flow rate as a function of pressure gradient is linear, as shown in Fig. 8 (b).

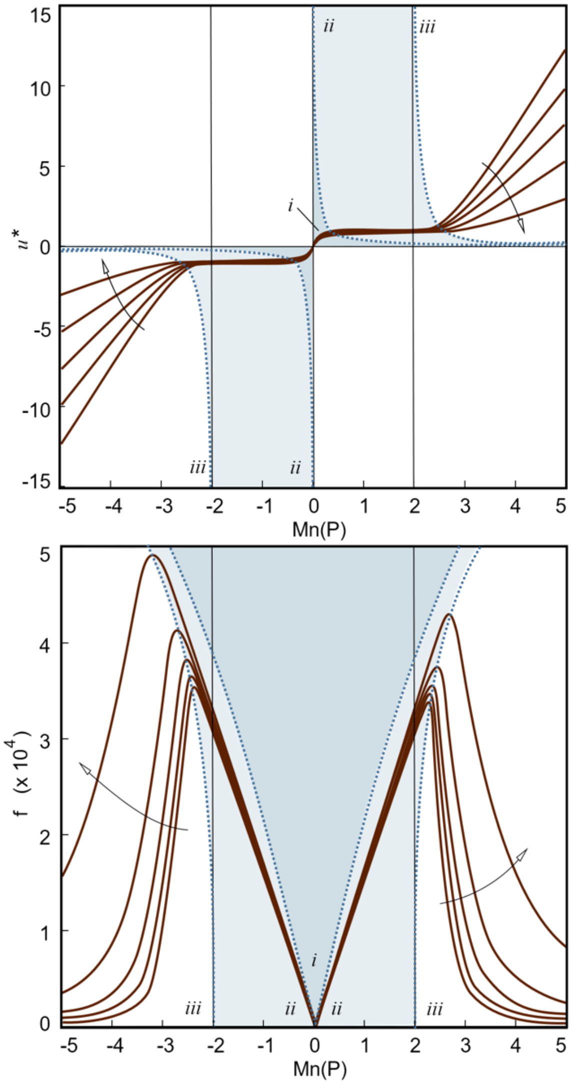

FIG. 9. (a) Ratio of volumetric loss to the nominal flow rate of a gear pump as a function of $Mn(p)$, for $Mn(\Omega)$ equal 0.5, 1, 1.5, 2, 2.5. The arrow indicates the direction $Mn(\Omega)$ increases. (b) Friction factor as a function of $Mn(p)$, for $Mn(\Omega)$ equal 0.5, 1, 1.5, 2, 2.5. The arrow indicates the direction $Mn(\Omega)$ increases. i: one-region mode; ii: two-region mode; iii: three-region mode. The dot lines indicate the transition for the velocity profile to transit from one mode to another.

C. Optimal Magnetic Field Intensity

Regarding the design of external gear pumps, we consider two performance metrics which evaluate the performance of dynamic seals. The first performance metric is given by the ratio of volumetric flow rate loss to the nominal volumetric flow rate of the gear pump. The nominal volumetric flow rate is proportional to the angular speed of the gear. Therefore, the dimensionless group $u^* = \dfrac{v}{R\Omega}$ can be used to characterize the sealing effectiveness of MR fluid, where v is the average velocity of the back-flow rate in the clearance of the gear pump, $R\Omega$ is proportional to the volumetric flow rate pumped by the gear pump. As shown in Fig. 9 (a), to achieve higher effectiveness, u^* should be designed to be as small as possible. $Mn(p)_{R1}$ is the transition point of the velocity profile from the one-region mode to the two-region mode for both slots, because $Mn(p)_{RS1}$ equals $Mn(p)_{RL1}$. $Mn(p)_{SR2}$, $Mn(p)_{LR2}$ are the transition points of the velocity profile from the two-region mode to the three-region mode for the slots in the presence of larger and smaller magnetic field intensity respectively. We find that when $Mn(p)$ is larger than $Mn(p)_{SR2}$, u^* dramatically increases. Thus, to ensure a small volumetric loss, $Mn(p)$ should be smaller than $Mn(p)_{SR2}$.

The second performance metric comes from the energy loss in both of the slots, which can be characterized by the friction factor $f = \dfrac{p}{\frac{1}{2}\rho v^2}$. To achieve the optimal sealing performance, the friction factor needs to be maximized, indicating that the back-flow between the gear teeth and the housing will experience as much energy loss as possible. As shown in Fig. 9 (b), the maximum friction factor

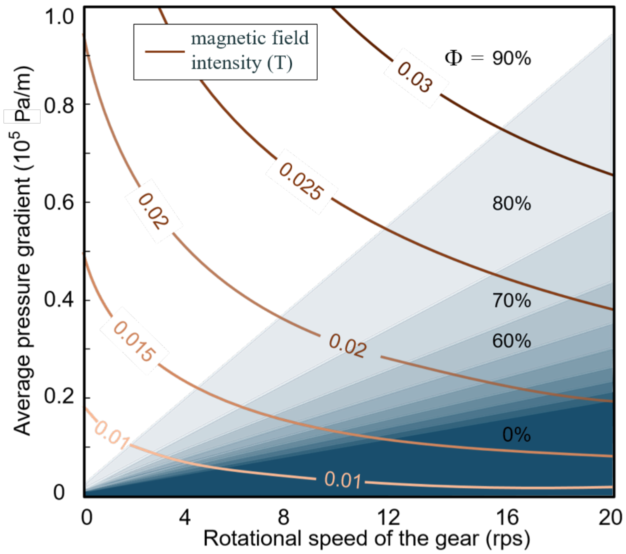

FIG. 10. Optimal magnetic field intensity (T). The solid lines indicate the magnetic field intensity distribution from 0.01 T to 0.03 T that one should select to minimize volumetric losses at a given rotational speed and pressure drop. Shaded area indicates the percentage of the reduction in volumetric loss from $\Phi = 90\%$ (white) to 0% (black).

can be achieved around $Mn(p)_{SR2}$, which is the $Mn(p)$ of the transition point from two-region mode to three-region mode for the slot in presence of the smaller magnetic field intensity.

Upon considering the two performance metrics, we find that the optimal sealing performance can be achieved at the transition of the two-region mode to the three-region mode. Thus, at any given nominal work condition of the external gear pump, the magnetic field intensity can be tuned to make the yield stress satisfy Eq. (13), which can be expressed explicitly by the following equation:

$$\tau_y = \frac{1}{2}\frac{\left(\frac{dp}{dx}\delta\right)^2 - 2\mu\frac{dp}{dx}R\Omega}{\frac{dp}{dx}\delta - \sqrt{2\mu\frac{dp}{dx}R\Omega}}. \tag{14}$$

The relationship between magnetic field intensity (B) and yield stress (Pa) of MR fluid has been studied in prior studies: [26]

$$\lg B = \frac{4}{7}\lg\tau_y + \frac{4}{7}\lg\left(9\times10^{-4}\right), \tag{15}$$

where B is the magnetic field intensity, τ_y is the yield stress.

We define a ratio Φ as a metric for the effectiveness of dynamic seals using MR fluid:

$$\Phi = \frac{Q_{Oil} - Q_{MR}}{Q_{Oil}}, \tag{16}$$

where Q_{Oil} is the volumetric loss using the Newtonian pump oil, Q_{MR} is the volumetric loss using MR fluid with the same viscosity as the Newtonian pump oil.

The optimal magnetic field intensity is shown in Fig. 10. It suggests that dynamic sealing using rheological fluid will achieve the optimal sealing effectiveness under a high pressure gradient and relatively low rotational speed, which would reduce the volumetric loss by over 90%.

IV. CONCLUSION

Volumetric loss accounts for a large portion of the extremely low efficiency of small-scale gear pumps. In order to reduce the volumetric loss without introducing larger friction, tighter manufacturing tolerances, or vulnerability to vibrations, we introduced a method where magnetorheological fluid is activated in the vicinity of the clearance between gear and housing to create a dynamic seal.

We verified the Bingham fluid model for MR fluids, and have accounted for the combined Poiseuille-Couette flow at low Reynolds number in the application of sealing in external gear pumps. We furthermore found four possible combinations of the velocity profiles given by two modified Mason numbers $Mn\,(p)$ and $Mn\,(\Omega)$.

We determined the dependence of optimal magnetic field intensity on the pressure gradient and rotational speed of the gear. The optimal magnetic field intensity corresponds to the transition for the velocity profile of MR fluid to transit from the three-region mode to the two-region mode. Our dynamic sealing method using MR fluid reduces volumetric loss above 90% when the pressure gradient is large; that is, when the hydraulic actuation system is under heavy load at low speed. Besides application for reducing the volumetric loss in the clearance, our method can also be applied for reducing the loss between the housing and the sides of gears for all types of gear pumps.

ACKNOWLEDGMENTS

A.E.H. acknowledges support from the Defense Advanced Research Projects Agency under grant number DARPA W31P4Q-13-1-0013. We gratefully thank Marie Baumier for insightful discussions.

Appendix A: Velocity profiles

Velocity profiles can be obtained analytically for all of the three types of modes for Bingham fluids. Based on Eqn. 6, the dimensionless form of the velocity profile $v^*(y^*)$ can be solved for by separating the variables and integrating from $y^*=0$ to $y^*=1$:

$$v^*(y^*) = -\frac{1}{2}Mn(\Omega)Mn(p)y^{*2} + U^* - Mn(\Omega)\left(\tau^*(y^*)|_{y^*=0} + sgn\left(\frac{du^*}{dy^*}\right)\right)y^* \tag{A1}$$

$$v^*(y^*) = -\frac{1}{2}Mn(\Omega)Mn(p)y^{*2} + \frac{1}{2}Mn(\Omega)Mn(p) - Mn(\Omega)\left(\tau^*(y^*)|_{y^*=0} + sgn\left(\frac{du^*}{dy^*}\right)\right)y^* + Mn(\Omega)\left(\tau^*(y^*)|_{y^*=0} + sgn\left(\frac{du^*}{dy^*}\right)\right). \tag{A2}$$

The velocity profile $v^*(y^*)$ close to and further away from the moving boundary are given by Eqn. A1 and Eqn. A2 respectively. The unknowns are the shear stress at the boundary $\tau^*(y^*)|_{y^*=0}$ and the locations which determine the region for the plug zone.

In the one-region mode, there is no plug zone. The velocity profile of a Bingham fluid is identical to that of a Newtonian fluid (see Fig. 6 (a) and (e)). When $0 \leq y^* \leq 1$,

$$v^*(y^*) = -\frac{1}{2}Mn(\Omega)Mn(p)y^{*2} + (-U^* + \frac{1}{2}Mn(\Omega)Mn(p))y^* + U^*. \tag{A3}$$

Integrating the velocity $v^*(y)$ over the cross-section gives the total flow rate. The average velocity of the fluid in the one-region mode is given by Eqn. 8.

Similarly, the velocity profile can be explicitly obtained in the two-region mode and three-region mode. For example, in the two-region mode, the Bingham model predicts two types of velocity profiles, depending on the direction of the pressure gradient and the moving boundary, as shown in Fig. 6 (b) (or(c)) and (f). Using the local frame xyz, we require that the shear stress $\tau = \pm\tau_y$ ($\tau^* = \pm 1$) at the boundary of the plug zone. In Fig. 6 (b) or (c), $Mn(\Omega) * Mn(p) < 0$ and the plug zone is attached to the stationary boundary. When $\sqrt{-2U^*/Mn(\Omega)Mn(P)} \leq y^* \leq 1$, $v^*=0$; when $0 \leq y^* < \sqrt{-2U^*/Mn(\Omega)Mn(P)}$,

$$v^*(y^*) = -\frac{1}{2}Mn(\Omega)Mn(p)y^{*2} + \frac{1}{2}\sqrt{-2Mn(\Omega)Mn(p)}y^* + U^*. \tag{A4}$$

In Fig. 6 (f), $Mn(\Omega) * Mn(p) < 0$ and the plug zone is attached to the moving boundary. When $0 \leq y^* \leq 1 - \sqrt{2U^*/Mn(\Omega)Mn(P)}$, $v^*(y^*) = U^*$; when

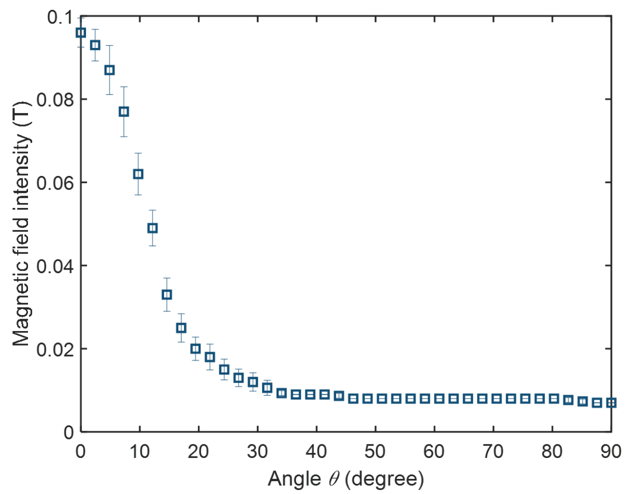

FIG. 11. Magnetic field intensity (T) as a function of θ (degree). Each point corresponds to the mean from three iterations of experiments, with error bars indicating standard deviation. θ is defined in Fig. 5. For $40^\circ < \theta < 90^\circ$, the error bars are smaller than the data point markers.

$1 - \sqrt{2U^*/Mn(\Omega)Mn(P)} < y^* \leq 1$,

$$v^*(y^*) = -\frac{1}{2}Mn(\Omega)Mn(p)y^{*2} - Mn(\Omega)Mn(p)(1-\sqrt{2U^*/Mn(\Omega)Mn(P)})y^* - Mn(\Omega)Mn(p)(1-\sqrt{2U^*/Mn(\Omega)Mn(P)}) - \frac{1}{2}Mn(\Omega)Mn(p). \tag{A5}$$

Integrating the velocity $v^*(y)$ over the cross-section gives the total flow rate. The average velocity of the fluid in the two-region mode is given by Eqn. 9 and Eqn. 10.

Appendix B: Parameter approximation and simulation

In order to determine the yield stress of the Bingham fluid as a function of θ (see Fig. 5) along the annular channels, we used a Hall effect Gauss/Tesla meter (Sypris 5100s) to measure the magnetic field intensity at 76 locations uniformly distributed along the annular channels at $r = 51$ mm. The sensitivity of the Gauss/Tesla meter is 0.001 T. To estimate the yield stress, we used the maximum absolute measured value as the magnitude of the magnetic field at each location (Fig. 11). Thus, in our simulation, we divided the annular channel into 76 elements. In each element, we approximated the magnetic field intensity to be constant; the yield stress τ_y was determined by the local magnetic field intensity as a function of θ [26].

In our simulation, we utilized two slots to approximate two annular channels, given that the aspect ratio $\delta/R = 2$

mm/50 mm $\ll 1$. To test this approximation, we compared the ratio of the flow rate in a slot Q_s to the flow rate in an annular channel Q_a, subject to the same pressure gradient and boundary condition. In the one-region mode, the velocity profile of a Bingham fluid is identical to that of a Newtonian fluid. In both cases, the flow rate in the one-region mode can be obtained analytically as the following:

$$Q_s = \frac{1}{\mu}\left(-\frac{\partial p}{\partial x}\right)\frac{(R_2-R_1)^3}{12} + \frac{1}{2}(\Omega_1 R_1 + \Omega_2 R_2)(R_2 - R_1), \tag{B1}$$

where Q_s is the flow rate of a Bingham fluid confined in a slot, μ is the viscosity of the MR fluid when no external magnetic field is present, $\frac{\partial p}{\partial x}$ is the pressure gradient, R_1 and R_2 are the radii of the inner cylinder and outer cylinder respectively, Ω_1 and Ω_2 are the rotational speed of the inner cylinder and outer cylinder respectively. The flow rate of a Bingham fluid confined in an annular channel in the one-region mode is given by:

$$\begin{aligned} Q_a =& \frac{1}{\mu}\frac{\partial p}{\partial \theta}\left[\frac{1}{4}r^2 \ln r - \frac{1}{4}r^2\right]_{r=R_1}^{r=R_2} \\ &+ \frac{1}{2}\frac{(\Omega_1 R_1^2 - \Omega_2 R_2^2) - (\alpha_1 R_1 - \alpha_2 R_2)}{R_1^2 - R_2^2} r^2 |_{R_1}^{R_2} \\ &+ \frac{(\Omega_1 - \Omega_2) - (\alpha_1/R_1 - \alpha_2/R_2)}{1/R_1^2 - 1/R_2^2} \ln r |_{R_1}^{R_2}, \end{aligned} \tag{B2}$$

where

$$\begin{aligned} \alpha_1 &= \frac{1}{\mu}\frac{\partial p}{\partial \theta}\left(\frac{1}{2}R_1 \ln R_1 - \frac{1}{4}R_1\right) \\ \alpha_2 &= \frac{1}{\mu}\frac{\partial p}{\partial \theta}\left(\frac{1}{2}R_2 \ln R_2 - \frac{1}{4}R_2\right). \end{aligned} \tag{B3}$$

We define a ratio ϵ as a metric for the error to account for the substitution of a slot channel for an annular channel:

$$\epsilon = \frac{Q_s - Q_a}{Q_a} \times 100\%. \tag{B4}$$

The ratio Q_s/Q_a as a function of the pressure gradient and the rotational speed of the inner disk is plotted in Fig. 12. As the pressure gradient increases, the error of the approximation approaches 2.0%. As the rotational speed of the disk increases, the error of the approximation decreases. Within the range of parameters used in our experiments, the error was within 2.0%. In this study, we opted to use slot approximation, because in the Cartesian coordinates, the flow rates of a Bingham fluid in Poiseuille-Coutte flow in all circumstances have analytical forms, which highlight the fluid physical behavior governed by the two Mason numbers $Mn(\Omega)$ and $Mn(p)$.

In our experiments, the total flow rate of the two slots were controlled by the syringe pump. Four groups of experiments were conducted with flow rates controlled to be 0.1 ml/min, 0.2 ml/min, 0.3 ml/min and 0.4 ml/min.

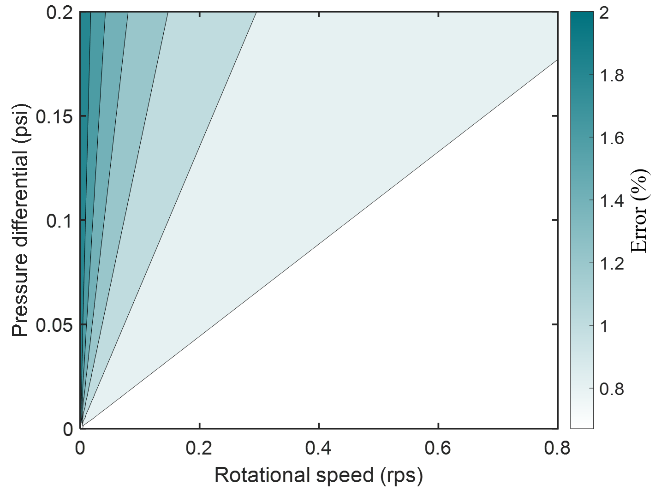

FIG. 12. Contour plot of the error ϵ (%) of using a slot approximation as a function of the pressure differential (psi) and rotational speed (rps).

In each group of experiments, we varied the rotational speed of the disk, ranging from 0 rps to 0.8 rps. In our simulation, to keep the total flow rate of the two slots to be constant, the pressure difference between the inlet and the outlet needed to be obtained as a function of the rotational speed of the disk. As shown in Eqn. 11, no explicit form of p^* as a function of $Mn(\Omega)$ can be obtained. We generated the total flow rates as a function of $Mn(\Omega)$ ranging from 0 rps to 0.8 rps and of pressure difference p ranging from 0 psi to 0.2 psi, and calculated the total flow rate for each combination of $Mn(\Omega)$ and p. We then explored the data set and searched for the total flow rate which was closest to 0.1 ml/min, 0.2 ml/min, 0.3 ml/min and 0.4 ml/min, and recorded the corresponding combination of the pressure difference and the rotational speed of the disk.

We take a numerical approach to calculate the velocity profile in the rectangular cross-section, and integrate the velocity profile in the cross-section to get the total flow rate. We first consider Couette flow as a simple example. In the case of two parallel infinite plates, the velocity decreases linearly away from the moving wall. In our experimental setup, as shown in Fig. 4 and Fig. 5, the channels are annular with a rectangular cross-section. The aspect ratio $h : \delta = 4$ mm: 2 mm= $2:1$ with a clearance 0.127 mm due to the gasket for sealing. We applied a finite element method to solve the boundary value problem of the Couette flow using Persson's code [45]. The ratio of the average velocity of the Couette flow confined in the channels of our experimental setup to that confined in two parallel infinite plates over the same height h is $0.241 : 0.5 = 0.482$. Pressure losses between the sensors and the inlet and outlet were taken into account. In our experiments, a significant pressure loss occurs due to the Poiseuille flow between the sensors and the inlet and outlet, four 90°-elbows and the cavities which con-

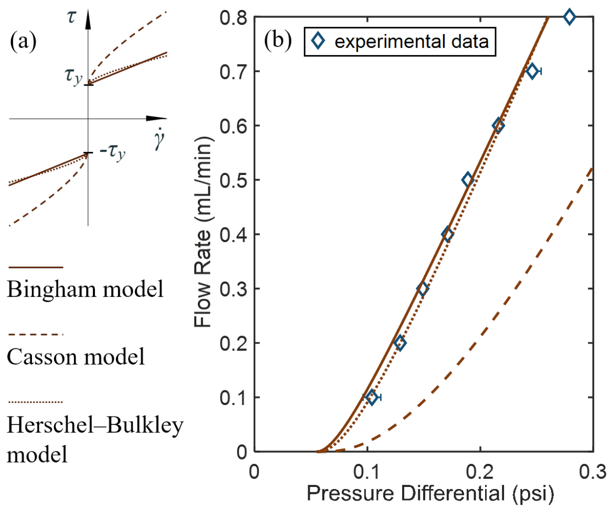

FIG. 13. Three types of models for MR fluids. (a) Shear stress τ versus shear rate $\dot{\gamma}$ for three types of viscoplastic models. (b) Experimental and theoretical results of Poiseuille flow of MR fluids. Pressure differential (psi) versus flow rate (ml/min).

nects the pitot tube and the two tubings. The distance between the pressure sensor and the outlet of the frame is $L_1 = 50$ mm, the distance between the outlet of the frame and the outlet of the channel is $L_2 = 38$ mm; the inner diameter of the tube is $d_1 = 3.0$ mm. The length of the tube fitting is $L_3 = 14$ mm; the inner diameter of the tube fitting is $d_2 = 2.1$ mm. The Reynolds number $Re_d = \frac{\rho U d}{\mu} \sim 10^{-3} \ll 1$, so inertial effects are negligible. For elbows, the pressure loss is estimated from an empirical equation using an equivelant length method [46]. In particular, for 90°-elbows, the equivalent length is $L_{eq} = 16d$ [46]. Hence, the additional pressure drop P_{loss} due to the tubing, the tube fitting and the elbows can be estimated as:

$$P_{loss} = \frac{128\mu Q}{\pi}\left(\frac{2L_1 + 2L_2 + 4L_{eq}}{d_1^4} + \frac{2L_3}{d_2^4}\right), \tag{B5}$$

where μ is the viscosity of the MR fluid when no external magnetic field is present, and Q is the flow rate controlled by the syringe pump.

Appendix C: Other models for MR fluids

Finally, we considered two alternate constitutive relationships, the Casson model and the Herschel-Bulkley model for MR fluids. Casson model is widely used for particle-laden fluids. In cardiovascular investigations, the Casson fluid model is capable of redicting the rheological behavior of blood in narrow arteries at low shear rates [47–50]; in the oil industry, researchers apply a modified Casson equation to model the rheological behavior of a waxy crude oil [51]. The constitutive relationship of Casson model is given by:

$$\begin{aligned} \sqrt{\tau_{yx}} = \sqrt{\tau_y} + \sqrt{\mu\dot{\gamma}};\, |\tau| > \tau_y \\ \dot{\gamma} = 0;\, |\tau| \le \tau_y, \end{aligned} \tag{C1}$$

where τ is the shear stress, τ_y is the yield stress, μ is the plastic viscosity, $\dot{\gamma}$ is the shear rate (see Fig. 13 (a)). Using the Cartesian coordinates xyz in Fig. 5, the velocity profile of the Poiseuille flow of a Casson fluid can be obtained analytically. When $0 \le y^* \le 1/2 - 1/Mn(p)$,

$$\begin{aligned} v^*(y^*) = &- \frac{Mn(\Omega)}{2Mn(p)}\left(Mn(p)y^* - \tau_0^*\right)^2 \\ &+ \frac{4Mn(\Omega)}{3Mn(p)}\left(-Mn(p)y^* + \tau_0^*\right)^{\frac{3}{2}} \\ &- \frac{Mn(\Omega)}{Mn(p)}\left(Mn(p)y^* + \tau_0^*\right) \\ &+ \frac{Mn(\Omega)}{Mn(p)}\left(\frac{\tau_0^{*2}}{2} - \frac{4\tau_0^{*\frac{3}{2}}}{3} + \tau_0^*\right), \end{aligned} \tag{C2}$$

where τ_0^* is the dimensionless shear stress at $y^* = 0$. Similarly, the velocity profile $v^*(y)$ can be computed when $1/2 - 1/Mn(p) \le y^* \le 1$.

The Herschel-Bulkley model provides a generalized model for a non-Newtonian fluid, especially for shear-thinning and shear-thickening fluids with a yield stress [52, 53]. The constitutive relationship is given by:

$$\begin{aligned} \tau_{yx} = \tau_y + K\dot{\gamma}^n;\, |\tau| > \tau_y \\ \dot{\gamma} = 0;\, |\tau| \le \tau_y, \end{aligned} \tag{C3}$$

where K is the consistency index, and n is the powerlaw index (see Fig. 13 (a)). Using the Cartesian coordinates xyz in Fig. 5, the velocity profile of the Poiseuille flow of a Herschel-Bulkley fluid can be obtained analytically. When $0 \le y^* \le 1/2 - 1/Mn(p)$,

$$\begin{aligned} v^*(y^*) = &- \frac{n}{n+1}\frac{Mn(\Omega_k)}{Mn(p)}\left(Mn(p)y^* + \tau_0^* - 1\right)^{\frac{n+1}{n}} \\ &+ \frac{n}{n+1}\frac{Mn(\Omega_k)}{Mn(p)}\left(\tau_0^* - 1\right)^{\frac{n+1}{n}}, \end{aligned} \tag{C4}$$

where τ_0^* is the dimensionless shear stress at $y^* = 0$, $Mn(\Omega_k)$ is redefined as:

$$Mn(\Omega_k) = \left(\frac{\tau_y}{K}\right)^{\frac{1}{n}} \frac{\delta}{R\Omega}. \tag{C5}$$

Similarly, the velocity profile $v^*(y)$ can be solved for when $\le 1/2 - 1/Mn(p) \le y^* \le 1$.

In order to test the alternative models for MR fluids, we compared the theoretical results with the experimental data under Poiseuille flow, as shown in Fig. 13 (b). The theoretical results predicted by Casson model deviate significantly from the experimental data. Using the Herschel-Bulkley model, we find $n = 0.985$, $K = 0.85\mu$

by fitting. The powerlaw index $n \approx 1$ indicates that the MR fluid in our study does not exhibit a significant shear-thinning or shear-thickening behavior. In light of these results, we retained the Bingham model for MR fluids in this investigation.

---

[1] F. Abhari, H. Jaafar, and N. A. M. Yunus, A comprehensive study of micropumps technologies, Int. J. Electrochem. Sci **7**, 9765 (2012).

[2] F. E. H. Tay, *Microfluidics and BioMEMS applications* (Springer, 2002).

[3] K. Junwu, Y. Zhigang, P. Taijiang, C. Guangming, and W. Boda, Design and test of a high-performance piezoelectric micropump for drug delivery, Sensors Actuators A Phys. **121**, 156 (2005).

[4] Q. Cui, C. Liu, and X. F. Zha, Study on a piezoelectric micropump for the controlled drug delivery system, Microfluid. Nanofluidics **3**, 377 (2007).

[5] H. T. G. v. Lintel, F. C. M. Pol, and S. Bouwstra, A piezoelectric micropump based on micromachining of silicon, Sensors and actuators **15**, 153 (1988).

[6] W. Y. Sim, H. J. Yoon, O. C. Jeong, and S. S. Yang, A phase-change type micropump with aluminum flap valves, J. Micromechanics Microengineering **13**, 286 (2003).

[7] K. H. Kim, H. J. Yoon, O. C. Jeong, and S. S. Yang, Fabrication and test of a micro electromagnetic actuator, Sensors Actuators A Phys. **117**, 8 (2005).

[8] K.-S. Yun, I.-J. Cho, J.-U. Bu, C.-J. Kim, and E. Yoon, A surface-tension driven micropump for low-voltage and low-power operations, J. microelectromechanical Syst. **11**, 454 (2002).

[9] A. Richter, A. Plettner, K. A. Hofmann, and H. Sandmaier, A micromachined electrohydrodynamic (EHD) pump, Sensors Actuators A Phys. **29**, 159 (1991).

[10] J.-H. Tsai and L. Lin, A thermal-bubble-actuated micronozzle-diffuser pump, J. microelectromechanical Syst. **11**, 665 (2002).

[11] A. Kargov, T. Werner, C. Pylatiuk, and S. Schulz, Development of a miniaturised hydraulic actuation system for artificial hands, Sensors Actuators A Phys. **141**, 548 (2008).

[12] X. Yang, C. Grosjean, and Y.-C. Tai, Design, fabrication, and testing of micromachined silicone rubber membrane valves, J. microelectromechanical Syst. **8**, 393 (1999).

[13] R. Rapp, W. K. Schomburg, D. Maas, J. Schulz, and W. Stark, LIGA micropump for gases and liquids, Sensors Actuators A Phys. **40**, 57 (1994).

[14] F. C. M. de Pol, H. T. G. Van Lintel, M. Elwenspoek, and J. H. J. Fluitman, A thermopneumatic micropump based on micro-engineering techniques, Sensors Actuators A Phys. **21**, 198 (1990).

[15] R. Zengerle, J. Ulrich, S. Kluge, M. Richter, and A. Richter, A bidirectional silicon micropump, Sensors Actuators A Phys. **50**, 81 (1995).

[16] M. Shen, C. Yamahata, and M. A. M. Gijs, A high-performance compact electromagnetic actuator for a PMMA ball-valve micropump, J. Micromechanics Microengineering **18**, 25031 (2008).

[17] S. Yao, D. E. Hertzog, S. Zeng, J. C. Mikkelsen, and J. G. Santiago, Porous glass electroosmotic pumps: design and experiments, J. Colloid Interface Sci. **268**, 143 (2003).

[18] D. S. Reichmuth, G. S. Chirica, and B. J. Kirby, Increasing the performance of high-pressure, high-efficiency electrokinetic micropumps using zwitterionic solute additives, Sensors Actuators B Chem. **92**, 37 (2003).

[19] J. Dpper, M. Clemens, W. Ehrfeld, S. Jung, K. P. Kaemper, and H. Lehr, Micro gear pumps for dosing of viscous fluids, J. Micromechanics Microengineering **7**, 230 (1997).

[20] G. E. Totten, *Handbook of hydraulic fluid technology* (CRC Press, 2011).

[21] H. E. Merritt, *Hydraulic control systems* (John Wiley & Sons, 1967).

[22] C. J. Hooke and E. Koc, End plate balance in gear pumps, Proc. Inst. Mech. Eng. Part B J. Eng. Manuf. **198**, 55 (1984).

[23] E. M. Furst and A. P. Gast, Particle dynamics in magnetorheological suspensions using diffusing-wave spectroscopy, Phys. Rev. E **58**, 3372 (1998).

[24] R. Tao and Q. Jiang, Structural transitions of an electrorheological and magnetorheological fluid, Phys. Rev. E **57**, 5761 (1998).

[25] Y. Zhu, E. Haddadian, T. Mou, M. Gross, and J. Liu, Role of nucleation in the structure evolution of a magnetorheological fluid, Phys. Rev. E **53**, 1753 (1996).

[26] M. R. Jolly, J. W. Bender, and J. D. Carlson, Properties and applications of commercial magnetorheological fluids, J. Intell. Mater. Syst. Struct. **10**, 5 (1999).

[27] F. D. Goncalves, J.-H. Koo, and M. Ahmadian, A review of the state of the art in magnetorheological fluid technologies-Part I: MR fluid and MR fluid models, Shock Vib. Dig. **38**, 203 (2006).

[28] J. M. Ginder, L. C. Davis, and L. D. Elie, Rheology of magnetorheological fluids: models and measurements, Int. J. Mod. Phys. b **10**, 3293 (1996).

[29] H.-S. Lee and S.-B. Choi, Control and response characteristics of a magneto-rheological fluid damper for passenger vehicles, J. Intell. Mater. Syst. Struct. **11**, 80 (2000).

[30] N. M. Kwok, Q. P. Ha, M. T. Nguyen, J. Li, and B. Samali, Bouc–Wen model parameter identification for a MR fluid damper using computationally efficient GA, ISA Trans. **46**, 167 (2007).

[31] K. Kim and D. Jeon, Vibration suppression in an MR fluid damper suspension system, J. Intell. Mater. Syst. Struct. **10**, 779 (1999).

[32] S. Sassi, K. Cherif, L. Mezghani, M. Thomas, and A. Kotrane, An innovative magnetorheological damper for automotive suspension: from design to experimental characterization, Smart Mater. Struct. **14**, 811 (2005).

[33] J.-H. Yoo and N. M. Wereley, Design of a high-efficiency magnetorheological valve, J. Intell. Mater. Syst. Struct. **13**, 679 (2002).

[34] N. Q. Guo, H. Du, and W. H. Li, Finite element analysis and simulation evaluation of a magnetorheological valve, Int. J. Adv. Manuf. Technol. **21**, 438 (2003).

[35] S. YOKOTA, K. YOSHIDA, and Y. KONDOH, in *Proc. JFPS Int. Symp. fluid power*, Vol. 1999 (1999) pp. 377–

380.
[36] M. Rowe, Measurements and computations of flow in pipe bends, J. Fluid Mech. **43**, 771 (1970).
[37] S. Melle, O. G. Caldern, M. A. Rubio, and G. G. Fuller, Microstructure evolution in magnetorheological suspensions governed by Mason number, Phys. Rev. E **68**, 41503 (2003).
[38] D. Du, E. Hilou, and S. L. Biswal, Modified Mason number for charged paramagnetic colloidal suspensions, Phys. Rev. E **93**, 62603 (2016).
[39] A. den Berg and L. Segerink, *Microfluidics for medical applications*, Vol. 36 (Royal Society of Chemistry, 2014).
[40] A. C. Becnel, W. Hu, and N. M. Wereley, Mason Number Analysis of a Magnetorheological Fluid-Based Rotary Energy Absorber, IEEE Trans. Magn. **50**, 1 (2014).
[41] A. C. Becnel, S. Sherman, W. Hu, and N. M. Wereley, Nondimensional scaling of magnetorheological rotary shear mode devices using the Mason number, J. Magn. Magn. Mater. **380**, 90 (2015).
[42] S. G. Sherman, A. C. Becnel, and N. M. Wereley, Relating Mason number to Bingham number in magnetorheological fluids, J. Magn. Magn. Mater. **380**, 98 (2015).
[43] K. Gjerstad, R. W. Time, and K. S. Bjrkevoll, Simplified explicit flow equations for Bingham plastics in Couette–Poiseuille flow–For dynamic surge and swab modeling, J. Nonnewton. Fluid Mech. **175**, 55 (2012).
[44] Y.-Q. Liu and K.-Q. Zhu, Axial Couette–Poiseuille flow of Bingham fluids through concentric annuli, J. Nonnewton. Fluid Mech. **165**, 1494 (2010).
[45] G. Strang, *Computational science and engineering*, Vol. 791 (Wellesley-Cambridge Press Wellesley, 2007).
[46] S. Menon, *Piping calculations manual* (McGraw Hill Professional, 2004).
[47] J. Venkatesan, D. S. Sankar, K. Hemalatha, and Y. Yatim, Mathematical analysis of Casson fluid model for blood rheology in stenosed narrow arteries, J. Appl. Math. **2013** (2013).
[48] K. Mukundakrishnan, P. S. Ayyaswamy, and D. M. Eckmann, Finite-sized gas bubble motion in a blood vessel: Non-Newtonian effects, Phys. Rev. E **78**, 36303 (2008).
[49] A. Iordan, A. Duperray, and C. Verdier, Fractal approach to the rheology of concentrated cell suspensions, Phys. Rev. E - Stat. Nonlinear, Soft Matter Phys. **77**, 2 (2008), arXiv:0709.3671.
[50] K. Ramesh and M. Devakar, Some analytical solutions for flows of Casson fluid with slip boundary conditions, Ain Shams Eng. J. **6**, 967 (2015).
[51] E. A. Kirsanov and S. V. Remizov, Application of the Casson model to thixotropic waxy crude oil, Rheol. acta **38**, 172 (1999).
[52] E. Mitsoulis, Flows of viscoplastic materials: models and computations, Rheol. Rev. **2007**, 135 (2007).
[53] D. Bonn, M. M. Denn, L. Berthier, T. Divoux, and S. Manneville, Yield stress materials in soft condensed matter, Rev. Mod. Phys. **89**, 35005 (2017).